HHS Public Access

Author manuscript

IEEE Access. Author manuscript; available in PMC 2025 April 25.

Published in final edited form as:

IEEE Access. 2024 ; 12: 116150–116161. doi:10.1109/access.2024.3446531.

Background Noise Removal in Non-Contrast- Enhanced Ultrasound Microvasculature Imaging Using Combined Collaborative, Morphological, and Vesselness Filtering

SOROOSH SABETI[1], **MOSTAFA FATEMI**[1] **[Life Fellow, IEEE]**, **AZRA ALIZAD**[1,2] **[Senior Member, IEEE]**

[1]Department of Physiology and Biomedical Engineering, Mayo Clinic College of Medicine and Science, Rochester, MN 55905, USA

[2]Department of Radiology, Mayo Clinic College of Medicine and Science, Rochester, MN 55905, USA

Abstract

Suppression of background noise in clutter filtered contrast-free ultrasound microvasculature images is an important step towards better visualization, accurate segmentation, and subsequent morphological analysis of vascular structures. While different approaches to tackling this problem have been proposed, the use of denoising and vessel-enhancing filters has proven to be a straightforward and effective scheme. In this paper, we propose a multi-stage background noise removal framework, suited to microvasculature images, comprising sequential implementation of three different modes of suppressing noise and intensifying vascular patterns, namely self-similarity based collaborative filtering, mathematical morphology based denoising, and Hessian based vessel enhancement. We evaluate the effects of each filtering stage in the framework using in-vitro phantom data and compare the denoising performance of the framework with a number of existing noise removal approaches, as well as the clutter filtered images in the absence of noise suppression techniques, using in-vivo data from human subjects. The results indicate that the suggested method is, in many cases, capable of complete background noise removal, zeroing out most background regions, and improving signal-to-noise ratio and contrast-to-noise ratio in other regions by tens of dB compared to the other methods.

INDEX TERMS

Contrast-free ultrasound; microvasculature imaging; background noise removal

Corresponding author: Azra Alizad (alizad.azra@mayo.edu).
MOSTAFA FATEMI and AZRA ALIZAD share senior authorship.

DISCLOSURE OF CONFLICT OF INTEREST

The authors do not have any potential financial interest related to the technology referenced in this paper.

I. INTRODUCTION

The advent of ultrafast ultrasound via plane wave imaging at high frame rates led to numerous technical advances in the field of ultrasound blood flow imaging without the use of contrast agents [1]. The ability to acquire long ensembles of ultrafast ultrasound data provides rich spatiotemporal ultrasound information that facilitates the separation of clutter signals and increases the Doppler sensitivity to slower flow enabling enhanced visualization of microvascular structures [1], [2]. Effective clutter filtering has facilitated microvessel imaging at sub-millimeter resolutions [3]. Without the help of contrast agents, investigators have developed a new ultrasound-based technique called quantitative high-definition microvessel imaging (qHDMI), visualizing microvessels at size scales as small as 150 microns and enabling extraction of vessel morphological features for quantification [4], [5], [6], [7]. Recently super resolution methods such as ultrasound localization microscopy (ULM), based on detection and tracking the trajectories of injected contrast agents, have shown great promise in visualization of sub-millimeter vessels in different organs [8], [9], [10], [11]. Nonetheless, longer acquisition time and the inherent need for injection of exogenous agents for contrast enhancement limit their practicality due to the associated availability and cost constraints, as well as technical challenges [12].

Contrast-free ultrasound microvessel imaging methods have seen many improvements in recent years. New methods such as qHDMI have shown great potential for visualization of micro-scale vasculature and quantification of morphological features of microvessels for cancer diagnosis and prognosis [13], [14], [15], [16], [17], [18], [19]. Though restricted in resolution by the fundamental diffraction limit, contrast-free ultrasound microvasculature imaging can offer accessible means of evaluation in clinical settings.

The process of vessel visualization in post-compounding plane-wave data generally begins with clutter filtering. Separation of tissue clutter from blood flow signals of interest can be achieved using singular value decomposition (SVD) [3], [20]. SVD-based methods differentiate clutter signals, which may potentially have overlapping frequency spectra with signals corresponding to slower flow, by removing the coherent eigenspace of the acquired data through a thresholding operation [21]. The choice of this threshold can have significant impact on the output. Therefore, several automatic threshold selection methods have been introduced for separation of the clutter and blood subspaces [4], [22].

Unwanted additive noise, however, remains as a part of the filtered data after removal of the coherent tissue subspace. The presence of this noise, which commonly presents as a background noise profile and mainly has electronic sources such as the time gain compensation (TGC) amplifiers, degrades the quality of the resulting vasculature image, lowering the signal-to-noise ratio (SNR) in the vicinity of target vessels, especially in deeper imaging regions, thus complicating vessel segmentation and quantification. A number of approaches have been introduced to address this problem. Assigning an eigenspace comprising the higher order singular values to the noise and subsequently thresholding out this subspace has been proposed [23]. Nevertheless, this can result in the removal of partially overlapping blood subspace. Another set of methods involve extracting a background noise profile for a given set of data acquisition settings using reference phantoms [23], and

transmission-less or open-air acquisitions [24], [25]. The problem with these methods is that they are not adaptive to variations in acquisition settings (frequency, TGC etc.). Adaptive background noise estimation and suppression methods, based on spatiotemporal correlation (STC) filtering [26], and axial downsampling and smoothing [27] have been recently proposed. However, STC filtering may fail to remove residual tissue signals which exhibit similar correlation characteristics as the flow signals, and axial downsampling can leave residual footprints of larger vessel structures which may result in smearing or deintensification of the vasculature.

Another approach to noise removal in ultrasound microvasculature images, is the isolated or combined use of denoising filters used with natural images. The use of self-similarity-based filters such as the non-local means (NLM) filter, morphological filters such as the top-hat filter (THF), and vessel enhancement filters such as the Frangi filter, has been investigated in the realm of non-contrast microvessel imaging [4], [28]. Alternative filters such as the block matching 3D (BM3D) [29] and its extensions such as BM3D-SH3D [30], bowler-hat filter (BHF) [31], and Jerman filter (JF) [32] in the aforementioned respective categories exist and have been utilized in ultrasound vessel imaging [33], [34], [35].

In this paper, we propose a multi-stage background noise removal algorithm. The proposed method is a filtering-based framework consisting of the combined usage of BM3D-SH3D, BHF, and JF as different modes of noise filtering (collaborative, morphological, and vesselness), specifically applicable for the purpose of denoising contrast-free ultrasound microvasculature images post-clutter-filtering. This approach is an extension of a previously introduced denoising framework employing NLM and THF [28]. We evaluate different stages of this method in denoising flow phantom data and demonstrate how this alternative framework enhances noise suppression in in-vivo data in terms of metrics including SNR, and contrast-to-noise ratio (CNR), compared to a number of other available denoising approaches. We demonstrate that this framework outperforms these noise removal approaches. The proposed method is a multi-stage sequential combination of off-the-shelf denoising and image quality enhancement filters, particularly suited to microvasculature imaging and applied to contrast-free ultrasound power Doppler imaging for the first time, to the best of our knowledge. Compared to the previously proposed method [28], the current framework replaces the NLM filter with the state-of-the-art self-similarity-based BM3D with sharpening (SH3D), improving the denoising performance and enhancing the separation of vessels around the edges. It then utilizes BHF, a morphological-based filter, better tailored for background noise removal in vasculature images, as compared to THF. And finally, it incorporates the hessian-based JF for targeted enhancement of vessel-shaped structures, and further suppression of background intensities.

II. MATERIALS AND METHODS

In this section, we present the details of the data sets used in this study to evaluate the performance of our proposed method. We then discuss the different stages of data processing to generate our noise-reduced microvasculature images. All the data processing and analyses were performed in MATLAB R2022b (Mathworks Inc., Natick, MA, USA).

A. FLOW PHANTOM DATA

A branched gelatin flow phantom (Volumetric Biotechnologies, Houston, Texas, USA) was used for this study. The vessel diameters are reported as 350±50 μm. An L22–14v transducer attached to the Vantage 256 research scanner (Verasonics, Kirkland, WA, USA), with the center frequency of 16.5 MHz was employed to acquire 500 frames of 11-angle compounded in-phase and quadrature (IQ) data at an effective frame rate of 1 KHz.

B. IN-VIVO DATA

Three different in-vivo data sets corresponding to a malignant breast lesion, a malignant thyroid nodule, and a cirrhotic liver, were also used for evaluation of our framework. All the data were collected under our institutional review board (IRB) approved protocols (IRB# 19–003028, IRB# 08–008778, IRB# 16–009435) with IRB approved informed consent signed by each participant. The studies were compliant with the Health Insurance Portability and Accountability Act (HIPAA). All the studies were conducted using the Alpinion Ecube12-R machine (ALPINION Medical Systems, Seoul, South Korea), in the plane-wave imaging mode. The L3–12H probe operating at 8.5 MHz was utilized for the breast lesion and thyroid nodule data, and the liver data were acquired using the SC1–4H probe operating at 3.6 MHz. The IQ data for each frame were generated and stored after coherent compounding of the 5-angle plane-wave acquisitions. Each acquisition contained 3 seconds of ~600 IQ frames per second.

C. MICROVASCULATURE VISUALIZATION AND THE DENOISING FRAMEWORK

Data processing for microvasculature visualization begins with clutter filtering. Clutter filtering is the process of separating the generally high intensity tissue clutter from the lower intensity signals generated by blood flow. We achieve this by implementing the SVD filter on the reshaped spatiotemporal ultrasound data, in the Casorati matrix format. The tissue clutter signals are typically assumed to be more coherent, thus constituting a low-rank subspace of the data. Consequently, by selecting a threshold, we can remove this subspace. In this work, we determine the clutter removal threshold for each data set by finding the point at which the second derivative of the singular value decay function (decay acceleration) falls below a threshold close to zero [4].

The clutter filtered data can then be utilized to visualize the vascular structure. To this end, we reshape the clutter-free reconstructed Casorati matrix back into the two-dimensional space by frame format and integrate the power of the data across the frame dimension to generate a power Doppler image. The resulting power Doppler image then contains signatures of blood flow (vessels) as well as the noise. At this point we employ our multi-stage denoising framework to suppress the remaining noise.

The framework consists of a sequential implementation of three filtering operations with three different noise suppressing mechanisms, the combined effect of which helps enhance the denoising process. These three filtering procedures include patch-based collaborative filtering using BM3D-SH3D, morphological filtering via BHF, and vessel enhancement filtering making use of JF. We begin by passing the clutter-filtered power Doppler image through the collaborative filtering stage (BM3D) of the algorithm to remove local noise

via transform filtering of self-similar patches. The image then undergoes the sharpening process (SH3D) which further isolates vessels around the edges. We then feed the result to a vessel-targeted morphological filtering algorithm (BHF) which in addition to removing background structures that do not fit a specified structuring element (similar to THF), retains only the vessel-like objects, which further enhances the background noise reduction. Finally, the Hessian-based vessel-enhancing filter (JF) suppresses most remaining noise elements by intensifying tubular/vessel-shaped structures. In the following subsections we briefly discuss how each of the filters in these stages of our algorithm operate.

D. BLOCK MATCHING 3D AND SHARPENING (BM3D-SH3D)

Block-matching and 3D filtering (BM3D) [29] is a state-of the-art self-similarity-based denoising method that has shown promise in the realm of medical imaging [36]. It follows the same principles of the non-local means (NLM) filter [37], in terms of grouping matching patches within the image. However, it enhances the noise removal process through a cascade of hard-thresholding and Wiener filtering in a 3D transform domain for each patch in an overall procedure denominated collaborative filtering [29]. The process of BM3D filtering consists of two main steps. In summary, the first step involves dividing the image into blocks/patches, grouping similar patches, applying a 3D transformation, hard thresholding in the transform domain, applying the inverse transformation, and aggregating the patches. In the second step, the very same procedure is applied to the original image, as well as the output of the first step. One key difference in the second step, however, is the replacement of hard thresholding with Wiener filtering, leading to an enhancement of the results of the first step. A variant of the BM3D was introduced in [30] through which denoising and sharpening of the images are achieved simultaneously via the addition of a method called alpha-rooting which helps in sharpening image details by amplifying portions of the spectrum in the transform domain. The block matching 3D with sharpening on the 3D spectra (BM3D-SH3D) in short involves the block matching, 3D transformation, hard thresholding, and alpha-rooting, after which the inverse 3D transformation and block aggregation is performed. SH3D refers to implementing the alpha-rooting (sharpening) process on the three-dimensional (spatio-blockstack) transform domain. Compared to application of sharpening on the two-dimensional transform spectrum, differential information in the blockstack/temporal dimension can also be leveraged for image sharpening. More details on this process can be found in [30]. BM3D-SH3D is particularly helpful in preserving and sharpening textures and edges [30]. The combined application of denoising and sharpening can help extract and separate out vessel structures and is thus used in this work. The codes used for this stage of our denoising framework are available online [38].

E. BOWLER-HAT FILTER (BHF)

Bowler-hat transform is a morphology-based technique that was introduced in [31] as a background suppression method in retinal images. It builds upon the fundamental concept of the top-hat filter (THF) in mathematical morphology which estimates the background profile through morphological opening using a structuring element. The bowler-hat filter (BHF) combines the use of disk structuring elements and line structuring elements to simultaneously estimate the background noise and enhance the elongated vessel-like

structures. More specifically, it performs opening on the image using a set of disk elements with diameters in number of pixels ranging from one to a specified threshold, generating an estimate of the background (which may contain larger segments, depending on the size of the element). Additionally, the opening is conducted using line elements with varying lengths and orientations. Pixel-wise maximum values across orientations are used at each length to generate an estimate of a vessel-enhanced image (which may also contain what would be deemed to be the background). The enhanced image at each element size (diameter/length) will be computed by subtracting the disk-opened image from the line-opened image, and the final output will be the pixel-wise maximum of this subtraction across all element sizes. The codes used for this stage of our denoising framework are available online [39].

F. JERMAN FILTER (JF)

Vessel-enhancing ("vesselness") filters are a set of filters designed to enhance and intensify tubular vessel-resembling structures in images. Many of these filters operate on Hessian-based local curvature analysis of structures which lead to simultaneous noise suppression and tube/vessel-like shape intensification, thereby enhancing the contrast of the vessels. One of the most commonly used of such filters is the Frangi filter [40], and the Jerman filter (JF) [32] is a relatively recently introduced variation of the vessel-enhancement filters with an improved vesselness function, which produces a more uniform response across different vessel sizes and local contrasts. In short, the JF, in a similar way to many other Hessian-based filters, works through applying a scale-dependent Gaussian-kernel-smoothed Hessian operator on the image and analysis of the eigenvalues of the Hessian matrix. The vesselness function, which is a function of these eigenvalues, will determine the local intensities based on the structural shapes. The Jerman vesselness function is devised such that it generates a normalized output, taking into account the ratio of the eigenvalues, and is robust to lower valued eigenvalues, thus resulting in a vessel-enhanced image that is more uniform and less susceptible to noise. Further details of this filter can be found in [32]. The codes used for this stage of our denoising framework are available online [41].

The flowchart of the different stages of our data processing framework is presented in Figure 1.

G. METRICS FOR PERFORMANCE EVALUATION

To evaluate the denoising performance of our proposed framework, we utilize two image quality metrics, namely signal-to-noise ratio (SNR), and contrast-to-noise ratio (CNR). SNR and CNR are commonly used to evaluate image quality in the context of blood flow and microvasculature imaging [23], [28]. These metrics are defined as presented in equations (1) to (2), respectively:

$$\mathrm{SNR} = 20\log_{10}\left(\frac{\bar{I}_{str}}{\sigma_N}\right), \tag{1}$$

$$\mathrm{CNR} = 20\log_{10}\left(\frac{\bar{I}_{str} - \bar{I}_{bg}}{\sigma_N}\right), \tag{2}$$

where $\bar{I}_{str}$ is the average intensity of the pels within the structure of interest (vessel), $\bar{I}_{bg}$ is the average pixel intensity in an area in the immediate vicinity of the target structure, and σn is the standard deviation of the noise (pixel intensities in a region devoid of vessels). In order to obtain these values, regions of interest (ROIs) are defined in the power Doppler images. Signal ROIs (shown as green dashed rectangles in the resulting figures) encompass a vessel structure and its vicinity. The vessel structure within the signal ROI is segmented (solid blue curves in the figures), the average pixel intensities of which determine $\bar{I}_{str}$. The mean intensity of the remaining pixels within the signal ROI results in $\bar{I}_{bg}$. Noise ROIs (white dashed rectangles) enclose an area where the presence of vessel structures is not expected. σn is the standard deviation of intensities within the noise ROI.

Additionally, for the purpose of resolution analyses, we make use of the full width at half maximum (FWHM) metric which indicates the width of a target structure (vessel) defined as the distance between the points on the intensity distribution across the structure where the intensities are half of its maximum amplitude.

III. RESULTS

In this section we evaluate the incremental improvement of each stage of our method and compare that against the “vanilla” SVD and the alternative stages included our previously proposed denoising framework (consisting of NLM and THF filtering), by implementing them on the flow phantom data, and then investigate the performance of our final framework against “undenoised” clutter-filtered data, previously proposed framework (NLM + THF), and three other methods, nicknamed last singular vector (LSV) based denoising, background noise suppression (BNS), and TGC compensation (TGCC), using in-vivo datasets described in the previous section. The LSV, BNS, and TGCC methods are implemented as described by the authors in [24], [26], and [27], respectively. These methods are examples of the state-of-the-art denoising methods for microvasculature imaging with different mechanisms of action, some of which are utilized in the more recent studies [42], [43], [44].

A. PARAMETER SWEEP FOR NLM AND BM3D-SH3D WITH FLOW PHANTOM DATA

Since NLM and BM3D-SH3D operate in a similar fashion, and filtering parameters can affect their performance, we applied these filters on our phantom data for a range of parameters to find their optimal settings. The range of values chosen for the sweep is based on the trend in output SNR and CNR values. The BM3D-SH3D’s noise standard deviation estimate (*Sigma*) and NLM’s filtering strength (*FS*) are the key parameters for which we evaluate our filtering results. Table 1 shows the SNR and CNR values for a *Sigma* range of [1, 33] for BM3D-SH3D and Table 2 shows these metrics for *FS* in the range of [0.001, 1] for NLM. The *Sigma* value of 31 for the BM3D-SH3D filter, and the *FS* value of 0.05 for the NLM filter had the best performance and were thus selected for further processing.

Figure 2 illustrates the CNR and SNR variations shown in Table 1 and Table 2, and Figure 3 depicts the results of implementing these denoising filters with their optimal parameters on the clutter filtered phantom data.

B. FLOW PHANTOM RESULTS

Figure 4 illustrates the power Doppler images of the branched flow phantom after clutter filtering using SVD. Figure 4(a) shows the flow image post-clutter-filtering before applying any denoising filter. Figures 4 (b) and (c) depict the clutter-filtered flow images following the use of NLM and BM3D-SH3D filters, respectively. The addition of THF to the NLM output and BHF to the output of BM3D-SH3D are shown in Figures 4 (d) and (e), respectively. Finally, the result combining BM3D-SH3D, BHF, and JF is presented in Figure 4 (f). The use of self-similarity-based filters on the post-SVD image, helps in reducing the noise as well as smoothing the background and the foreground (Figures 4 (b) and (c)). Compared to NLM, BM3D-SH3D better separates the vessels from the background and intensifies the intra-vessel pixel intensities compared to the background. The use of morphological filters (THF and BHF) improves the background intensity suppression (Figures 4 (d) and (e)). This is more noticeable with the use of BHF, as it enhances the elongated vessel shapes, and is reflected in SNR and CNR values. The use of the JF suppresses the background noise to the lowest possible level, such that the intensity values at most pixels outside the area of the target vessels are set to zero.

Table 3 shows the SNR and CNR values for all of the subfigures of Figure 2. for the given regions of interest delineated in the images. “Inf” entries indicate infinite values resulting from the absolute zero pixel intensities in the selected noise ROI.

Figure 5 shows the intensity profile for the various filter combination results across the solid cyan line in Figure 4. The calculated FWHM for the SVD, NLM, BM3D-SH3D, NLM + THF, BM3D-SH3D + BHF, and BM3D-SH3D + BHF + JF are 0.56, 0.56, 0.28, 0.28, 0.28, and 0.28 mm respectively.

C. IN-VIVO RESULTS

Figure 6 shows the denoising results for a malignant breast lesion. Table 4 shows the SNR and CNR values for all of the subfigures of Figure 6 for the given regions of interest delineated in the images. Figure 7 depicts the intensity profile for the results using the compared methods (SVD, SVD + NLM + THF, SVD + LSV, SVD + BNS, SVD + TGCC, and SVD + BM3D-SH3D + BHF + JF) across the solid cyan line in Figure 6. The calculated FWHM values for the SVD, SVD + NLM + THF, SVD + LSV, SVD+BNS, SVD+TGCC, and SVD+BM3D-SH3D + BHF + JF methods are 1.34 mm, 0.85 mm, 1.30 mm, 1.18+mm, 1.18 mm, and 0.37 mm respectively.

Figure 8 illustrates the results of implementing the proposed method on a malignant thyroid nodule data set. Table 5 shows the SNR and CNR values for all of the subfigures of Figure 8 for the given regions of interest delineated in the images. Finally, Figure 9 depicts the noise suppression results for a cirrhotic liver. And Table 6 shows the SNR and CNR values for all of the subfigures of Figure 9 for the given regions of interest delineated in the images.

D. VESSEL SEGMENTATION AND BACKGROUND NOISE FLOOR ESTIMATION

To further demonstrate the importance of background noise suppression with the proposed framework, we evaluate the difference in vessel segmentation results among the compared methods using an adaptive binarization method. This method determines the threshold for binarization based on the first-order statistics in a neighborhood around each pixel [45]. Figure 10 shows the binarized images for the liver data set. It can be observed in Figure 10 (f) that vessels are better segmented and vessel diameters are better maintained. Additionally, at the edges of the masked liver capsule, a rim of segmented pixels is generated in all the other subfigures. However, with zeroed out pixels in the background using the proposed method, such a rim is not observed.

For the purpose of noise floor estimation, we begin by removing the vessel structures from the power Doppler images generated by each method. This is achieved by removing the vessel pixels as determined by the segmentation in Figure 10 (f). The average intensity of the remaining pixels is defined as the noise floor. The average background noise intensities (noise floor) for each of the compared methods are shown in Figure 11 for the breast lesion data set in (a), the thyroid nodule data set in (b), and the cirrhotic liver data set in (c). A significant decrease in noise floor is observed using the proposed method.

IV. DISCUSSION

With the improvements in clutter filtering, particularly SVD-based methods implemented on information-rich spatiotemporal data in ultrafast ultrasound acquisitions, additive noise, comprising signals emanating from sources other than blood flow, is a challenge that needs to be dealt with. Enhanced noise, especially in deeper imaging regions, can at times dominate the local dynamic range of the image, leading to difficulties in finding suitable binarization thresholds for vessel segmentation, thereby impacting the quantitative analyses of vessel structures. The purpose of this paper was to introduce a multi-stage denoising framework, employing different noise-suppressing filters with different mechanisms of action, particularly suited to microvessel imaging. In particular, the goal here was to improve upon our previously introduced denoising approach (NLM + THF) [28] for further background noise suppression. The results of the proposed approach were compared against the clutter filtered data without any denoising, as well as several existing denoising approaches in a number of in-vivo data sets acquired from human subjects, in terms of SNR and CNR. Depending on the selected noise region, the proposed method can achieve zeroed out noise floors, leading to SNR and CNR values approaching infinity. This occurs due to the extensive background noise suppression after vessel enhancement such that background intensities are set to zero across the image. Furthermore, vessel segmentation results using an adaptive thresholding method, demonstrate the utility of the proposed method in facilitating isolation of vessel structures. Vessel segmentation (binarization) is a key step in preparation of microvasculature images for subsequent morphological analysis and quantification. Results presented in Figure 10, show how the extensive denoising achieved by the proposed method can preclude the inclusion of spurious structures in the binarized imaged through an automated adaptive thresholding method, without necessitating manual threshold selection (which would be subjective and data dependent). Additionally,

around the edges of masked structures (such as the boundaries of the masked liver capsule), a rim of pixels can be generated due to the sharp variation in background intensities, while this can be avoided using the proposed method (Figure 10 (f)). Noise floor analyses also indicate how much the background noise intensities are reduced using the proposed method, compared to the other denoising approaches.

The proposed method in this paper consists of three different modes of denoising, namely self-similarity based collaborative denoising, mathematical morphology based denoising, and vesselness based denoising. In our previously introduced method, the NLM filter was utilized as a self-similarity patch based denoising method. BM3D is an expansion of the NLM filter which works on the same principles but makes use of inherent sparsities in transform domains. Since introduction, BM3D has been considered a state-of-the-art denoising method and a reference standard for many new denoising algorithms. It has also shown superior denoising performance to NLM in medical imaging applications [34], [46]. Image sharpening, a joint enhancement incorporated in the BM3D-SH3D algorithm used in this study, can be employed to further isolate blood vessels, and has shown promise in vessel imaging [47]. It is worth noting that the term “3D” in the BM3D-SH3D algorithm refers to the processing nature of the algorithm as applied on a three-dimensional transform domain. Otherwise, the application of the proposed method is on two-dimensional images. The BHF step involved in our method is also an extension of the THF, whereby combinations of structuring elements help in enhancement of vessel-like structures and can therefore be a more fitting alternative to THF in vascular imaging. The use of BHF in ultrasound microvessel imaging has already been investigated and shown merit [35]. The last stage of our proposed framework involves Hessian-based vessel enhancement. Methods based on this approach have been widely used in vessel imaging applications [48], [49]. The well-known Frangi filter has been successfully used in ultrasound microvasculature imaging [4]. The use of JF as an alternative to the Frangi filter helps create a more uniform vessel response, thus reducing the generation of artifact structures in the background.

Our study has limitations. The proposed denoising method contains a series of filtering operations, each of which requiring a set of parameters to be selected before processing. The parameter tuning is heavily data-dependent, and in common scenarios where a large batch of different data sets need to be processed at once, parameter sweep to find an optimal combination is not a feasible option. Another drawback of this method is that its application is restricted to vessel imaging as its morphological and vesselness operations are aimed at enhancing vessel-like structures. In many applications of ultrasound flow and perfusion imaging, the signals and structures of interest are not limited to the elongated vessel shapes. Finally, the proposed framework was only evaluated on a limited number of in-vivo data sets. The impact of the enhanced noise suppression on quantifying the morphological features of the vasculature, with the end goal of improving microvasculature imaging as a complementary diagnostic tool was beyond the scope of this study and requires further investigation in future studies.

V. CONCLUSION

In this paper, we presented a denoising method comprising collaborative, morphological, and vesselness filtering operations, with application to contrast-free ultrasound microvasculature imaging. We investigated its performance in noise removal of flow phantom and various in-vivo data sets against a set of existing denoising frameworks, as well as the case where no denoising is employed post-clutter-filtering. The results showed noise suppression in terms of SNR, and CNR can be improved by tens of dB and can even approach infinity with most background regions where noise intensity is reduced to zero. These improvements have the potential of enhancing quantitative microvasculature imaging methods, which requires further exploration in future studies.

ACKNOWLEDGMENT

The authors would like to acknowledge Dr. Pouya Metanat for his help in data acquisition of flow phantom.

This work was supported by the National Institutes of Health under Grant R01CA239548 and Grant R01 EB017213.

This work involved human subjects or animals in its research. Approval of all ethical and experimental procedures and protocols was granted by the Mayo Clinic Institutional Review Board (IRB) under Application Nos. 19-003028, 08-008778, and 16-009435, and performed in line with the Health Insurance Portability and Accountability Act (HIPAA).

Biographies

SOROOSH SABETI received the B.S. and M.S. degrees in electrical engineering from the Ferdowsi University of Mashhad, Mashhad, Iran, in 2012 and 2014, respectively, and the Ph.D. degree in electrical and computer engineering from The University of Utah, Salt Lake City, UT, USA, in 2020. He is currently a Senior Research Fellow with Mayo Clinic College of Medicine and Science, Rochester, MN, USA. His research interests include signal processing, image processing, machine learning, and their applications in acoustic, ultrasonic, and medical signal and image analysis.

MOSTAFA FATEMI (Life Fellow, IEEE) received the Ph.D. degree in electrical engineering from Purdue University. He joined the Mayo Clinic College of Medicine and Science, Rochester, MN, USA, in 1994, where he is currently a Professor of biomedical engineering with the Department of Physiology and Biomedical Engineering. At the

Mayo Clinic College of Medicine and Science, he is also an Active Member with the Mayo Clinic Cancer Center and the Center for Clinical and Translational Science. His current research interests include developing novel ultrasonic methods for cancer imaging, microvasculature imaging, and bladder function evaluation. His research program has been continuously supported by multiple major federal grants from the National Institute of Health (NIH), National Science Foundation (NSF), Department of Defense, and the Komen Breast Foundation for the Cure. He holds fellow membership at these institutions: American Institute of Medical and Biological Engineering (AIMBE), Acoustical Society of America (ASA), and American Institute of Ultrasound in Medicine (AIUM). He was a recipient of the IEEE-UFFC Distinguished Lecturer Award.

AZRA ALIZAD (Senior Member, IEEE) received the medical degree from Tehran University Medical Sciences. She received a fellowship from Tehran University Medical Sciences. She is currently a Professor of radiology with the Department of Radiology and a Professor of biomedical engineering and an Associate Professor of medicine with the Mayo Clinic College of Medicine and Science, Rochester, MN, USA. At the Mayo Clinic, she is also an Active Member of the Mayo Clinic Cancer Center and the Center for Clinical and Translational Science. In addition to her training in medicine, she has a broad background and expertise in medical ultrasound. She directs the Translational Ultrasound Research Laboratory, involving development and application of novel ultrasound technologies, such as microvasculature imaging, functional ultrasound, elastography, vibro-acoustic imaging for diagnosis of abnormalities in breast, thyroid, prostate, neck masses, and axillary lymph nodes, brain, and bone. She is the Principal Investigator of multiple major federal grants funded by the National Institute of Health (NIH) and a recipient of grant funded by Komen Breast Foundation for the Cure. She is an Elected Fellow of American Institute for Medical and Biological Engineering (AIMBE) and American Institute of Ultrasound in Medicine (AIUM) and a Senior Member of Institute of Electrical and Electronics Engineers-UFFC.

REFERENCES

[1]. Tanter M and Fink M, “Ultrafast imaging in biomedical ultrasound,” IEEE Trans. Ultrason., Ferroelectr., Freq. Control, vol. 61, no. 1, pp. 102–119, Jan. 2014. [PubMed: 24402899]

[2]. Osmanski B-F, Pezet S, Ricobaraza A, Lenkei Z, and Tanter M, “Functional ultrasound imaging of intrinsic connectivity in the living rat brain with high spatiotemporal resolution,” Nature Commun., vol. 5, no. 1, p. 5023, Oct. 2014.

[3]. Demené C, Deffieux T, Pernot M, Osmanski B-F, Biran V, Gennisson J-L, Sieu L-A, Bergel A, Franqui S, Correas J-M, Cohen I, Baud O, and Tanter M, “Spatiotemporal clutter filtering of ultrafast ultrasound data highly increases Doppler and fUltrasound sensitivity,” IEEE Trans. Med. Imag, vol. 34, no. 11, pp. 2271–2285, Nov. 2015.

[4]. Bayat M, Fatemi M, and Alizad A, “Background removal and vessel filtering of noncontrast ultrasound images of microvasculature,” IEEE Trans. Biomed. Eng, vol. 66, no. 3, pp. 831–842, Mar. 2019. [PubMed: 30040621]

[5]. Ghavami S, Bayat M, Fatemi M, and Alizad A, "Quantification of morphological features in non-contrast-enhanced ultrasound microvasculature imaging," IEEE Access, vol. 8, pp. 18925–18937, 2020. [PubMed: 32328394]

[6]. Ternifi R, Wang Y, Polley EC, Fazzio RT, Fatemi M, and Alizad A, "Quantitative biomarkers for cancer detection using contrast-free ultrasound high-definition microvessel imaging: Fractal dimension, Murray's deviation, bifurcation angle & spatial vascularity pattern," IEEE Trans. Med. Imag, vol. 40, no. 12, pp. 3891–3900, Dec. 2021.

[7]. Adusei S, Ternifi R, Fatemi M, and Alizad A, "Custom-made flow phantoms for quantitative ultrasound microvessel imaging," Ultrasonics, vol. 134, Sep. 2023, Art. no. 107092.

[8]. Couture O, Besson B, Montaldo G, Fink M, and Tanter M, "Microbubble ultrasound super-localization imaging (MUSLI)," in Proc. IEEE Int. Ultrason. Symp, Oct. 2011, pp. 1285–1287.

[9]. Desailly Y, Pierre J, Couture O, and Tanter M, "Resolution limits of ultrafast ultrasound localization microscopy," Phys. Med. Biol, vol. 60, no. 22, pp. 8723–8740, Nov. 2015. [PubMed: 26509596]

[10]. Beliard B, Ahmanna C, Tiran E, Kanté K, Deffieux T, Tanter M, Nothias F, Soares S, and Pezet S, "Ultrafast Doppler imaging and ultrasound localization microscopy reveal the complexity of vascular rearrangement in chronic spinal lesion," Sci. Rep, vol. 12, no. 1, p. 6574, Apr. 2022. [PubMed: 35449222]

[11]. Lin F, Shelton SE, Espíndola D, Rojas JD, Pinton G, and Dayton PA, "3-D ultrasound localization microscopy for identifying microvascular morphology features of tumor angiogenesis at a resolution beyond the diffraction limit of conventional ultrasound," Theranostics, vol. 7, no. 1, pp. 196–204, 2017. [PubMed: 28042327]

[12]. Martin KH and Dayto PA, "Current status and prospects for microbubbles in ultrasound theranostics," Interdiscipl. Rev., Nanomedicine Nanobiotechnology, vol. 5, no. 4, pp. 329–345, 2013.

[13]. Ternifi R, Wang Y, Gu J, Polley EC, Carter JM, Pruthi S, Boughey JC, Fazzio RT, Fatemi M, and Alizad A, "Ultrasound high-definition microvasculature imaging with novel quantitative biomarkers improves breast cancer detection accuracy," Eur. Radiol, vol. 32, no. 11, pp. 7448–7462, Apr. 2022. [PubMed: 35486168]

[14]. Gu J, Ternifi R, Larson NB, Carter JM, Boughey JC, Stan DL, Fazzio RT, Fatemi M, and Alizad A, "Hybrid high-definition microvessel imaging/shear wave elastography improves breast lesion characterization," Breast Cancer Res, vol. 24, no. 1, pp. 1–13, Mar. 2022. [PubMed: 34983617]

[15]. Gu J, Ternifi R, Sabeti S, Larson NB, Carter JM, Fazzio RT, Fatemi M, and Alizad A, "Volumetric imaging and morphometric analysis of breast tumor angiogenesis using a new contrast-free ultrasound technique: A feasibility study," Breast Cancer Res, vol. 24, no. 1, pp. 1–15, Nov. 2022. [PubMed: 34983617]

[16]. Sabeti S, Ternifi R, Larson NB, Olson MC, Atwell TD, Fatemi M, and Alizad A, "Morphometric analysis of tumor microvessels for detection of hepatocellular carcinoma using contrast-free ultrasound imaging: A feasibility study," Frontiers Oncol., vol. 13, Apr. 2023, Art. no. 1121664.

[17]. Kurti M, Sabeti S, Robinson KA, Scalise L, Larson NB, Fatemi M, and Alizad A, "Quantitative biomarkers derived from a novel contrast-free ultrasound high-definition microvessel imaging for distinguishing thyroid nodules," Cancers, vol. 15, no. 6, p. 1888, Mar. 2023. [PubMed: 36980774]

[18]. Adusei SA, Sabeti S, Larson NB, Dalvin LA, Fatemi M, and Alizad A, "Quantitative biomarkers derived from a novel, contrast-free ultrasound, high-definition microvessel imaging for differentiating choroidal tumors," Cancers, vol. 16, no. 2, p. 395, Jan. 2024. [PubMed: 38254884]

[19]. Ferroni G, Sabeti S, Abdus-Shakur T, Scalise L, Carter JM, Fazzio RT, Larson NB, Fatemi M, and Alizad A, "Noninvasive prediction of axillary lymph node breast cancer metastasis using morphometric analysis of nodal tumor microvessels in a contrast-free ultrasound approach," Breast Cancer Res, vol. 25, no. 1, pp. 1–11, Jun. 2023. [PubMed: 36597146]

[20]. Nayak R, Lee J, Chantigian S, Fatemi M, Chang S-Y, and Alizad A, "Imaging the response to deep brain stimulation in rodent using functional ultrasound," Phys. Med. Biol, vol. 66, no. 5, Mar. 2021, Art. no. 05LT01.

[21]. Tierney J, Coolbaugh C, Towse T, and Byram B, “Adaptive clutter demodulation for non-contrast ultrasound perfusion imaging,” IEEE Trans. Med. Imag, vol. 36, no. 9, pp. 1979–1991, Sep. 2017.

[22]. Baranger J, Arnal B, Perren F, Baud O, Tanter M, and Demené C, “Adaptive spatiotemporal SVD clutter filtering for ultrafast Doppler imaging using similarity of spatial singular vectors,” IEEE Trans. Med. Imag, vol. 37, no. 7, pp. 1574–1586, Jul. 2018.

[23]. Song P, Manduca A, Trzasko JD, and Chen S, “Ultrasound small vessel imaging with block-wise adaptive local clutter filtering,” IEEE Trans. Med. Imag, vol. 36, no. 1, pp. 251–262, Jan. 2017.

[24]. Song P, Manduca A, Trzasko JD, and Chen S, “Noise equalization for ultrafast plane wave microvessel imaging,” IEEE Trans. Ultrason., Ferroelectr., Freq. Control, vol. 64, no. 11, pp. 1776–1781, Nov. 2017. [PubMed: 28880169]

[25]. Sabeti S, Nayak R, McBane RD, Fatemi M, and Alizad A, “Contrast-free ultrasound imaging for blood flow assessment of the lower limb in patients with peripheral arterial disease: A feasibility study,” Sci. Rep, vol. 13, no. 1, p. 11321, Jul. 2023. [PubMed: 37443250]

[26]. Nayak R, Fatemi M, and Alizad A, “Adaptive background noise bias suppression in contrast-free ultrasound microvascular imaging,” Phys. Med. Biol, vol. 64, no. 24, 2019, Art. no. 245015.

[27]. Chinchilla L, Frappart T, Fraschini C, Correas J-M, and Gennisson J-L, “Resistivity index mapping in kidney based on ultrasensitive pulsed-wave Doppler and automatic spectrogram envelope detection,” IEEE Trans. Ultrason., Ferroelectr., Freq. Control, vol. 70, no. 3, pp. 207–218, Mar. 2023. [PubMed: 37022223]

[28]. Adabi S, Ghavami S, Fatemi M, and Alizad A, “Non-local based denoising framework for in vivo contrast-free ultrasound microvessel imaging,” Sensors, vol. 19, no. 2, p. 245, Jan. 2019. [PubMed: 30634614]

[29]. Dabov K, Foi A, Katkovnik V, and Egiazarian K, “Image denoising by sparse 3-D transform-domain collaborative filtering,” IEEE Trans. Image Process, vol. 16, no. 8, pp. 2080–2095, Aug. 2007. [PubMed: 17688213]

[30]. Dabov K, Foi A, Katkovnik V, and Egiazarian K, “Joint image sharpening and denoising by 3D transform-domain collaborative filtering,” in Proc. Int. TICSP Workshop Spectral Meth. Multirate Signal Process, Sep. 2007, pp. 1–24.

[31]. Sazak C, Nelson CJ, and Obara B, “The multiscale bowler-hat transform for blood vessel enhancement in retinal images,” Pattern Recognit, vol. 88, pp. 739–750, 2019.

[32]. Jerman T, Pernus F, Likar B, and Špiclin Ž, “Enhancement of vascular structures in 3D and 2D angiographic images,” IEEE Trans. Med. Imag, vol. 35, no. 9, pp. 2107–2118, Sep. 2016.

[33]. Demené C, Robin J, Dizeux A, Heiles B, Pernot M, Tanter M, and Perren F, “Transcranial ultrafast ultrasound localization microscopy of brain vasculature in patients,” Nature Biomed. Eng, vol. 5, no. 3, pp. 219–228, Mar. 2021. [PubMed: 33723412]

[34]. Lei S, Zhang G, Zhu B, Long X, Jiang Z, Liu Y, Hu D, Sheng Z, Zhang Q, Wang C, Gao Z, Zheng H, and Ma T, “In vivo ultrasound localization microscopy imaging of the Kidney’s microvasculature with block-matching 3-D denoising,” IEEE Trans. Ultrason., Ferroelectr., Freq. Control, vol. 69, no. 2, pp. 523–533, Feb. 2022. [PubMed: 34727030]

[35]. Qiu X-R, Wang M-T, Huang H, Kuo L-C, Hsu H-Y, Yang T-H, Su F-C, and Huang C-C, “Estimating the neovascularity of human finger tendon through high-frequency ultrasound micro-Doppler imaging,” IEEE Trans. Biomed. Eng, vol. 69, no. 8, pp. 2667–2678, Aug. 2022. [PubMed: 35192458]

[36]. Mohd Sagheer SV and George SN, “A review on medical image denoising algorithms,” Biomed. Signal Process. Control, vol. 61, Aug. 2020, Art. no. 102036.

[37]. Buades A, Coll B, and Morel J-M, “Non-local means denoising,” Image Processing Line, vol. 1, pp. 208–212, Jul. 2011.

[38]. Lemaitre G. (2016). BM3D. [Online]. Available: https://github.com/glemaitre/BM3D

[39]. (2019). Bowler-Hat-2D. [Online]. Available: https://github.com/CigdemSazak/bowler-hat-2d

[40]. Frangi AF, Niessen WJ, Vincken KL, and Viergever MA, “Multiscale vessel enhancement filtering,” in Proc. 1st Int. Conf, 1998, pp. 130–137.

[41]. Jerman T. (2018). Enhancement Filter. [Online]. Available: https://github.com/timjerman/JermanEnhancementFilter

[42]. Kou Z, Lowerison M, You Q, Wang Y, Song P, and Oelze ML, “High-resolution power Doppler using null subtraction imaging,” IEEE Trans. Med. Imag, vol. 1, no. 1, pp. 1–24, Apr. 2024.

[43]. Lowerison MR, Sekaran NVC, Dong Z, Chen X, You Q, Llano DA, and Song P, “Super-resolution ultrasound reveals cerebrovascular impairment in a mouse model of Alzheimer’s disease,” J. Neurosci, vol. 44, no. 9, Jan. 2024, Art. no. e1251232024.

[44]. Lowerison MR, Sekaran NVC, Zhang W, Dong Z, Chen X, Llano DA, and Song P, “Aging-related cerebral microvascular changes visualized using ultrasound localization microscopy in the living mouse,” Sci. Rep, vol. 12, no. 1, p. 619, Jan. 2022. [PubMed: 35022482]

[45]. Bradley D and Roth G, “Adaptive thresholding using the integral image,” J. Graph. Tools, vol. 12, no. 2, pp. 13–21, 2007.

[46]. Hanchate V and Joshi K, “MRI denoising using BM3D equipped with noise invalidation denoising technique and VST for improved contrast,” SN Appl. Sci, vol. 2, pp. 1–8, Jul. 2020.

[47]. Ozkava U, Ozturk S, Akdemir B, and Sevfi L, “An efficient retinal blood vessel segmentation using morphological operations,” in Proc. 2nd Int. Symp. Multidisciplinary Stud. Innov. Technol, 2018, pp. 1–20.

[48]. Fraz MM, Remagnino P, Hoppe A, Uyyanonvara B, Rudnicka AR, Owen CG, and Barman SA, “Blood vessel segmentation methodologies in retinal images—a survey,” Comput. Methods Programs Biomed, vol. 108, no. 1, pp. 407–433, 2012. [PubMed: 22525589]

[49]. Lamy J, Merveille O, Kerautret B, Passat N, and Vacavant A, “Vesselness filters: A survey with benchmarks applied to liver imaging,” in Proc. 25th Int. Conf. Pattern Recognit, 2020, pp. 1–20.

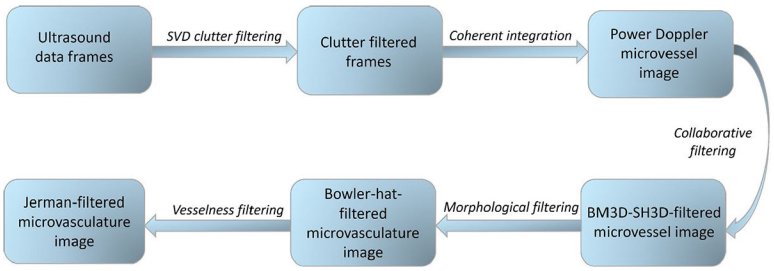

FIGURE 1.
The flowchart of the microvasculature visualization and denoising process.

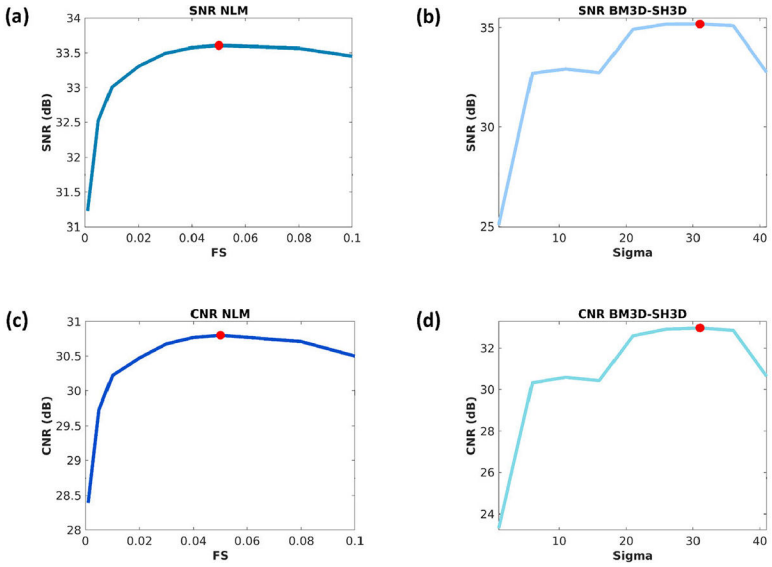

FIGURE 2.

SNR and CNR value plots for a range of *Sigma* and *FS* parameters for the BM3D-SH3D and NLM filters. Red circles indicate the point at which each metric is maximized.

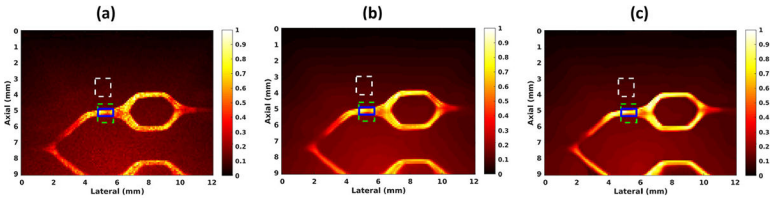

FIGURE 3.

The denoising results for the flow phantom data (a) after SVD (b) SVD + NLM (c) SVD + BM3D-SH3D for their corresponding optimal parameters (*Sigma* = 31 for BM3D-SH3D, and *FS* = 0.05 for NLM). Dashed green and white rectangles indicate the signal and noise ROIs, and the blue area delineates the segmented target vessel within the signal ROI.

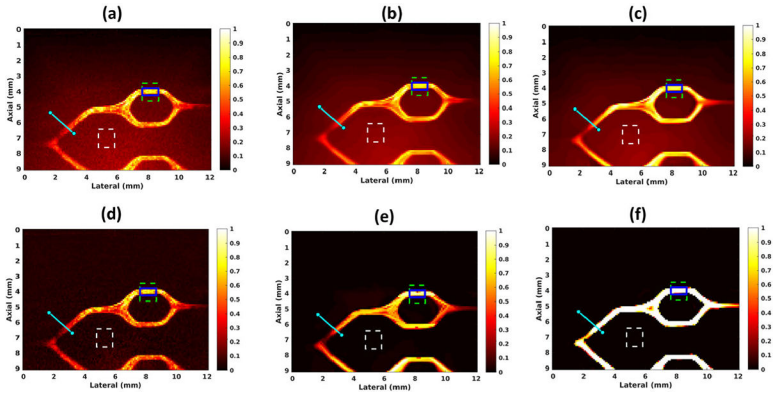

FIGURE 4.

The denoising results for the flow phantom data (a) after SVD (b) SVD + NLM (c) SVD + BM3D-SH3D (d) SVD + NLM + THF (e) SVD + BM3D-SH3D + BHF (f) SVD + BM3D-SH3D + BHF + JF (proposed method). Dashed green and white rectangles indicate the signal and noise ROIs, and the blue area delineates the segmented target vessel within the signal ROI. The solid cyan line shows the cross-section over which the intensity profiles are evaluated.

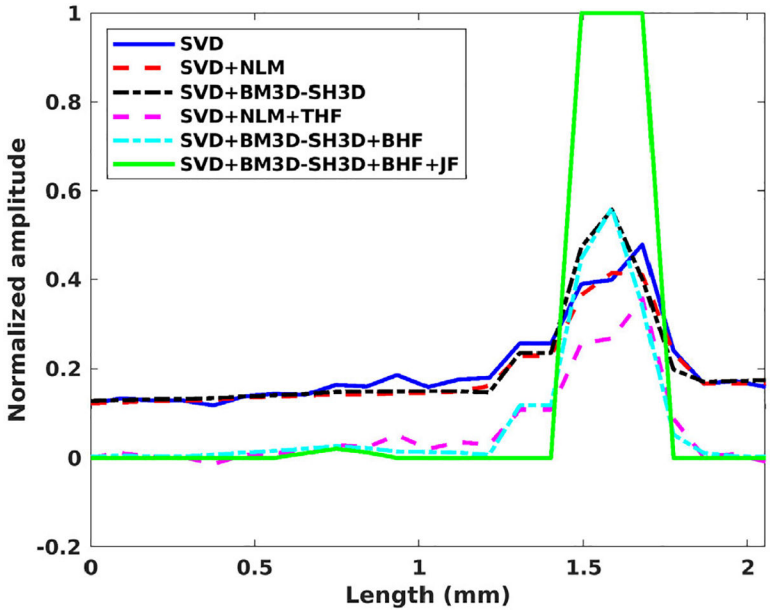

FIGURE 5.
Intensity profiles across the solid cyan line in Figure 4.

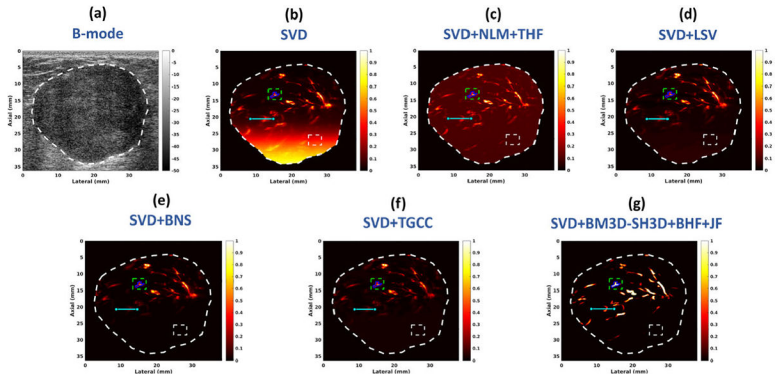

FIGURE 6.

The denoising results for the malignant breast lesion data (a) B-mode (b) after SVD (c) SVD + NLM + THF (d) SVD + LSV (e) SVD + BNS (f) SVD + TGCC (f) SVD + BM3D-SH3D + BHF + JF. White dashed line delineates the boundaries of the lesion. Dashed green and white rectangles indicate the signal and noise ROIs, and the blue area delineates the segmented target vessel within the signal ROI. The solid cyan line shows the cross-section over which the intensity profiles are evaluated.

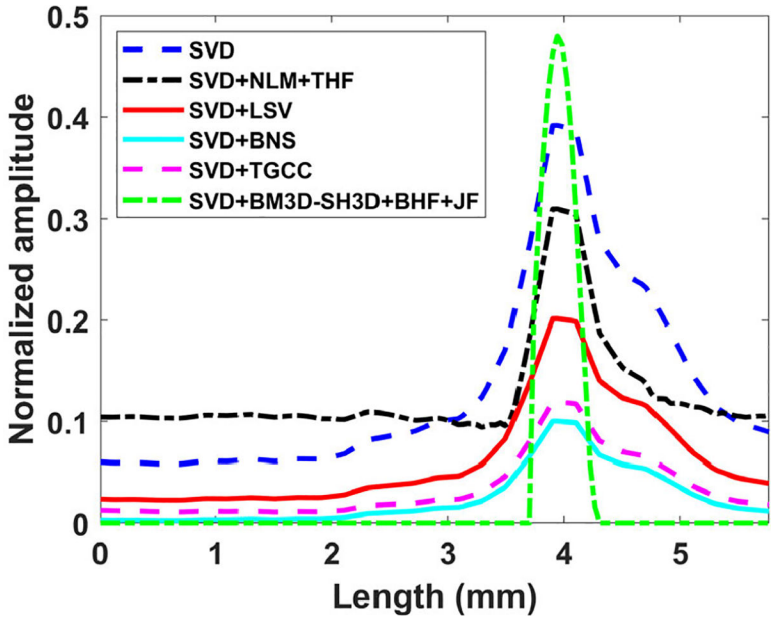

FIGURE 7.
Intensity profiles across the solid cyan line in Figure 6.

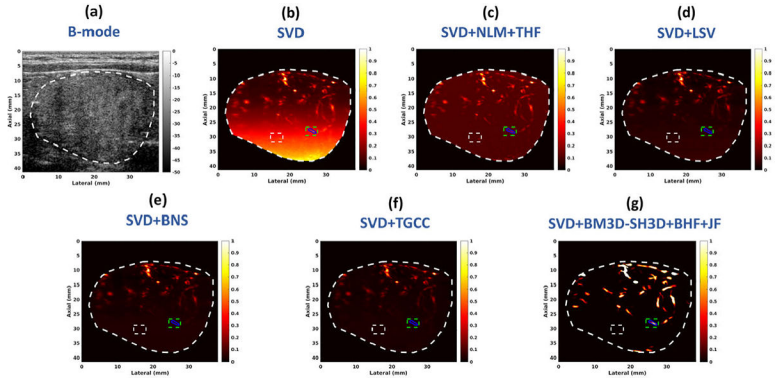

FIGURE 8.

The denoising results for the malignant thyroid nodule data (a) B-mode (b) after SVD (c) SVD + NLM + THF (d) SVD + LSV (e) SVD + BNS (f) SVD + TGCC (f) SVD + BM3D-SH3D + BHF + JF (proposed method). White dashed line delineates the boundaries of the nodule. Dashed green and white rectangles indicate the signal and noise ROIs, and the blue area delineates the segmented target vessel within the signal ROI.

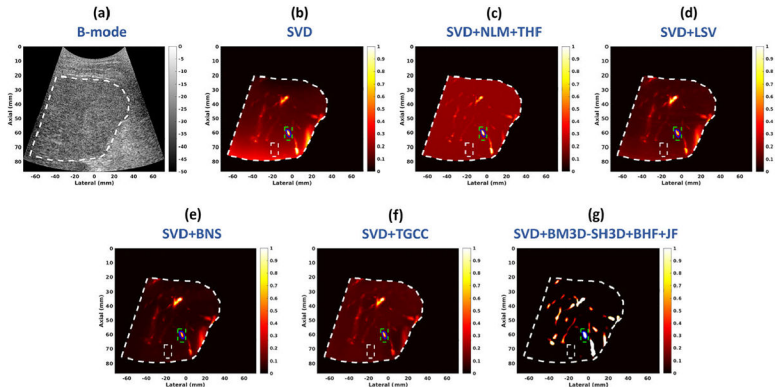

FIGURE 9.

The denoising results for the cirrhotic liver data (a) B-mode (b) after SVD (c) SVD + NLM + THF (d) SVD + LSV (e) SVD + BNS (f) SVD + TGCC (f) SVD + BM3D-SH3D + BHF + JF (proposed method). White dashed line delineates the boundaries of the liver capsule. Dashed green and white rectangles indicate the signal and noise ROIs, and the blue area delineates the segmented target vessel within the signal ROI.

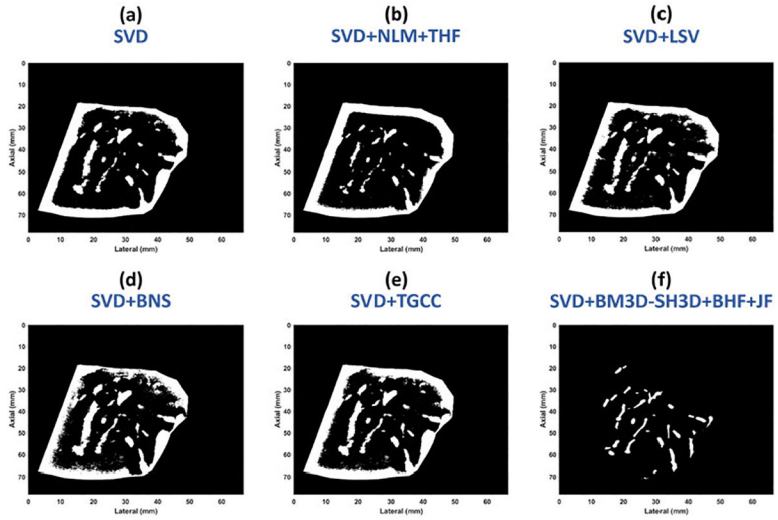

FIGURE 10.

Vessel segmentation results for the liver data set after (a) SVD, and denoising with (b) SVD + NLM + THF, (c) SVD + LSV (d) SVD + BNS, (e) SVD + TGCC, and (f) SVD + BM3D-SH3D + BHF + JF(proposed method).

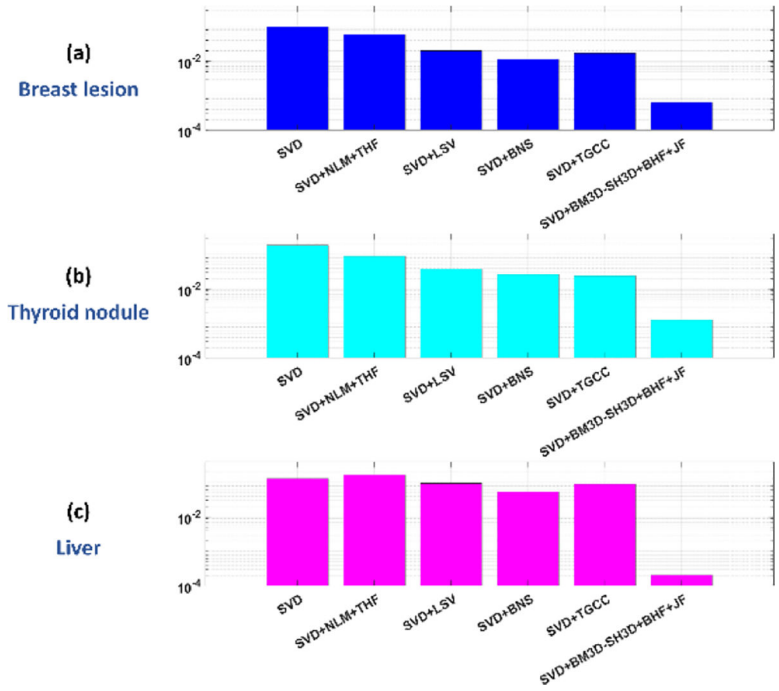

FIGURE 11.

Average background noise intensities for the (a) breast lesion, (b) thyroid nodule, and (c) liver data sets. The intensities are presented in log scale in the vertical axis of each plot.

TABLE 1.

SNR and CNR values for different *Sigma* values in denoising using BM3D-SH3D.

Sigma	**1**	**6**	**11**	**16**	**21**	**26**	**31**	**36**	**41**
SNR (dB)	24.36	32.08	32.63	32.54	33.74	34.95	34.99	34.95	32.65
CNR(dB)	22.57	29.58	30.26	30.18	31.40	32.60	32.71	32.68	30.48

TABLE 2.

SNR and CNR values for different *FS* values in denoising using NLM.

FS	**0.001**	**0.005**	**0.01**	**0.02**	**0.03**	**0.04**	**0.05**	**0.08**	**0.1**
SNR (dB)	31.22	32.52	33.01	33.31	33.49	33.58	33.61	33.57	33.45
CNR(dB)	28.39	29.73	30.22	30.47	30.68	30.77	30.80	30.71	30.50

TABLE 3.

SNR and CNR values for different denoising stages for the phantom data results as shown in Figure 4.

	SVD	SVD + NLM	SVD + BM3D-SH3D	SVD + NLM + THF	SVD + BM3D-SH3D + BHF	SVD + BM3D-SH3D + BHF + JF
SNR (dB)	16.02	16.38	16.62	28.79	46.35	Inf
CNR (dB)	13.31	13.78	14.12	28.14	45.71	Inf

TABLE 4.

SNR and CNR values for the breast lesion denoising results as shown in Figure 6.

	SVD	SVD + NLM + THF	SVD + LSV	SVD + BNS	SVD + TGCC	SVD + BM3D-SH3D + BHF + JF
SNR (dB)	9.31	26.60	33.19	45.81	39.80	Inf
CNR (dB)	7.85	22.40	31.80	44.91	38.65	Inf

TABLE 5.

SNR and CNR values for the thyroid nodule denoising results as shown in Figure 8.

	SVD	SVD + NLM + THF	SVD + LSV	SVD + BNS	SVD + TGCC	SVD + BM3D-SH3D + BHF + JF
SNR (dB)	12.94	15.39	14.70	16.69	16.10	31.44
CNR (dB)	−2.44	5.78	3.13	6.94	6.53	31.19

TABLE 6.

SNR and CNR values for the cirrhotic liver denoising results as shown in Figure 9.

	SVD	SVD + NLM + THF	SVD + LSV	SVD + BNS	SVD + TGCC	SVD + BM3D-SH3D + BHF + JF
SNR (dB)	15.68	19.23	20.41	26.53	22.42	Inf
CNR (dB)	11.76	14.86	17.50	24.66	19.69	Inf